A discrete spectral model for intermediate crack debonding in FRP-strengthened RC beams

Rui Sun, Enrique Sevillano, Ricardo Perera

A B S T R A C T

One of the common failure modes of reinforced concrete (RC) beams strengthened in flexure with a bonded fibre-reinforced polymer (FRP) is intermediate crack (IC) debonding, which is originated at a critical section in the vicinity of flexural cracks and propagates to a plate end. Despite considerable research over the last years, few reliable and simplified IC debonding strength models have been developed. This paper firstly presents a one-dimensional model based on the discrete crack approach for concrete and the spectral element method for the numerical simulation of the IC debonding process. The progressive formation of flexural cracks and subsequent concrete–FRP interfacial debonding is formulated by the introduction of a new element able to represent both phenomena simultaneously without perturbing the numerical procedure. Furthermore, with the proposed model, high frequency dynamic response for these kinds of structures can also be obtained in a very simple and non-expensive way, which makes this procedure very useful as a tool for diagnoses and detection of debonding in its initial stage by monitoring the change in local dynamic characteristics.

1. Introduction

Since the early 1990s the external bonding of fibre reinforced polymer (FRP) plates or sheets has emerged as a popular method for the strengthening of reinforced concrete (RC) structures [1–3]. Composite materials offer several advantages for engineering applications that require a combination of high strength and stiffness with low weight. However, this kind of strengthening often leads to brittle failure modes induced by a debonding originated at the plate end (either plate end debonding or concrete cover rip-off) or induced by an intermediate crack (IC). In this last case, debonding initiates at a major flexural crack and then propagates towards a plate end. However, in spite of it being the dominant failure mode in certain circumstances, such as thin FRP plates, the number of studies regarding the IC debonding mechanism is limited. An extensive review of the existing studies on the numerical modelling of debonding failures in FRP-plated RC members has recently been conducted by Chen [4]. Most studies are based on refined 2D and 3D finite element (FE) simulations using the smeared-crack approach [5–9]. The differences among the different proposals are mainly related to the bond behaviour adopted between concrete and internal steel reinforcement and between FRP and concrete and to the modelling of concrete cracking. The discrete crack approach has also been used in FE analyses [10,11] although less frequently because of its limitations. However, although the accuracy reached by using FE models is high in some proposals, the high computational cost of structural response analyses based on FE models such as the ones referred to above has prompted the development of less expensive numerical procedures for the analysis and design of FRP-strengthened RC structures. With this purpose, Smith and Gravina [12] presented a local deformation model solved via the finite difference method to simulate IC debonding. Liu et al. [13] proposed a numerical partial-interaction model to simulate the same phenomenon. Faella et al. [14] proposed a one-dimensional model based on a similar one proposed by the same authors for steel–concrete composite beams [15]. More recently, Barbato [16] developed a nonlinear beam FE model, based on the Euler–Bernoulli kinematic assumptions and the fibre section model, to estimate the load-carrying capacity of RC beams flexurally strengthened with FRP strips and plates. However, IC debonding was not specifically considered.

It is the purpose of this work to implement a one-dimensional simplified numerical model that for practical applications can truly represent the structural response of flexural FRP-strengthened concrete beams. In [17], a 1D spectral model based on the Timoshenko theory and using a smeared-crack approach was developed for simulating the behaviour of reinforced concrete beams externally

strengthened by FRP materials. Spectral methods [18,19] are a suitable high order technique to solve problems to high accuracy in a simple domain, such as that corresponding to the strengthened beam, allowing significant reductions in the computational load. At lower accuracies, they demand less computer memory than the FE alternative since they allow obtaining the same accuracy as low-order methods (like finite elements) by using a reduced number of grid points, thus giving rise to a significant saving of computational resources. However, the smeared crack model is subjected to some limitations. In this approach, the geometry remains fixed and, therefore, as displacement continuity is maintained across a crack, the distribution of strains in regions adjacent to cracks, which is a key factor controlling debonding failures in FRP-strengthened RC structures, can be overlooked. To have a more realistic prediction of the distribution and to be able to investigate the effect of mode-II fracture, a discrete crack model is formulated, which allows displacement discontinuity across a crack and uses both mode-I and mode-II crack prediction criteria. The discrete crack approach is employed to consider geometrical discontinuities such as flexural cracks and debonding of the FRP sheet, originated from the tip the flexural crack. This model is able to provide a sound mechanical description and interpretation of the phenomena leading to failure of FRP-retrofitted RC beams in a very simple way and with low computational cost.

Because the spectral matrix is stiffness formulated, it can be assembled in a completely analogous way to that used for the FEM. Thus, the assembly feature of the FEM can be equally applied to the spectral stiffness matrix method. In this sense, the proposed new element is formulated in such a way that when a geometrical discontinuity appears, one only needs to replace the original spectral element with the new spectral element with embedded crack, keeping the original nodes unaltered. Hence, the insertion of this element in a modular approach is suitable for faster modelling since the perturbation on the original mesh is minor. Furthermore, to avoid the assumption of a previous crack pattern, the size of the elements is chosen considering different evaluation formulas of the mean crack spacing.

Another advantage of the proposed method is its ability to suitably represent the dynamic behaviour of FRP-strengthened RC structures placing a special focus on the influence of the interfacial intermediate debonding mechanism on the mentioned behaviour. Due to the local nature of the debonding phenomenon, the study of its dynamic effect on the behaviour of an FRP-strengthened structure requires working with high frequencies. Traditional methods, such as the finite element method, would need extremely large mesh sizes to capture very short wavelengths, which might become prohibitive from the computational point of view. Simplified methods need to be established for practical design applications. With the spectral element method [20], however, inertial properties are modelled exactly and, therefore, few elements are necessary to capture very accurate solutions at the highest frequencies in large regions. This gives the method a strong potential to be applied to the dynamic behaviour study of FRP-strengthened structures in the presence of debonding.

The applicability of the proposed method is discussed by comparing the analysis results with the experimental results obtained from static four-point loading tests conducted by Matthys [21]. A subsequent study has also been carried out to check the feasibility of the proposed method as a tool to solve problems involving dynamic analysis.

2. FRP-strengthened RC beam fully bonded

Firstly, the model for an FRP-strengthened beam intact with respect to debonding, i.e. the adhesive is fully bonded to the concrete beam and to the FRP layer, is introduced. This model will be presented in a summarised way since it was previously introduced in [17]. Three layers including the concrete beam, the adhesive layer and the FRP strip are used to represent the structure. The three layers are modelled independently and are then joined together by using compatibility relations. To do this, a form of the displacement field is assumed through the entire height of the strengthened beam as follows

$$u_C(x,z,t) = u_0(x,t) - z\phi(x,t) \tag{1}$$

$$u_F(x,z,t) = u_0(x,t) - z\phi(x,t) + s(x,t) \tag{2}$$

$$w(x,z,t) = w(x,t) \tag{3}$$

where u_C, u_F and w are the axial displacements in RC beam and FRP plate and the transverse displacement at a material point, respectively, $u_0(x, t)$ is the midplane axial displacement, ϕ is the curvature-independent rotation of the beam cross-section about the Y-axis, z is the coordinate measured from the mid-plane and s is the interface-slip, which can be expressed as

$$s = u_{F\ top} - u_{C\ bot} \tag{4}$$

with $u_{F\ top}$ and $u_{C\ bot}$ denoting the axial displacements at the top of the FRP plate and at the bottom of the RC beam, respectively.

The strains are computed applying the linear strain–displacement relations to Eqs. (1)–(4). The shear strain in the adhesive $\gamma_{xz\ AD}$ can be calculated from the interface-slip s and its thickness e_{AD}

$$\gamma_{xz\ AD} = s/e_{AD} \tag{5}$$

Eq. (5) represents a simplification of the reality of variable shear strain through the adhesive thickness in the bond-critical zones.

Although other more complex models have been proposed in the literature [22] to represent the concrete–FRP interface by using cohesive elements, one of the main objectives of the present work is the development of a simplified model able to give suitable results in practical applications with low computational cost.

The governing equations for the four unknown variables, u_0, w, ϕ and s, of motion, are derived using Hamilton's principle for the assumptions above [17]

$$\delta u_0:\ I_0\ddot{u}_0 - I_1\ddot{\phi} + I_{0FRP}\ddot{s} - A_{11}u_{0,xx} + B_{11}\phi_{,xx} - A_F s_{,xx} = 0 \tag{6}$$

$$\delta w:\ I_0\ddot{w} - A_{22}w_{,xx} + A_{22}\phi_{,x} = 0 \tag{7}$$

$$\delta\phi:\ I_2\ddot{\phi} - I_1\ddot{u}_0 - I_{1F}\ddot{s} + B_{11}u_{0,xx} - D_{11}\phi_{,xx} - A_{22}w_{,x} + A_{22}\phi + B_F s_{,xx} = 0 \tag{8}$$

$$\delta s:\ I_{0F}\ddot{s} + I_{0F}\ddot{u}_0 - I_{1F}\ddot{\phi} - A_F s_{,xx} - A_F u_{0,xx} + B_F\phi_{,xx} + \frac{G_{AD}sb_{AD}}{e_{AD}} = 0 \tag{9}$$

and the four associated natural boundary equations are

$$N = A_{11}u_{0,x} - B_{11}\phi_{,x} + A_F s_{,x} \tag{10}$$

$$V = A_{22}w_{,x} - A_{22}\phi \tag{11}$$

$$M = -B_{11}u_{0,x} + D_{11}\phi_{,x} - B_F s_{,x} \tag{12}$$

$$N^* = A_F s_{,x} + A_F u_{0,x} - B_F\phi_{,x} \tag{13}$$

where $\ddot{()}$ represents double differentiation with respect to t and $()_{,xx}$ represents double differentiation with respect to x. N, V, M and N^* are the stress resultants associated with the variables u_0, w, ϕ and s, respectively. A_{11}, B_{11}, D_{11}, A_{22}, A_F and B_F are the stiffness coefficients and I_0, I_1 and I_2 are the inertial coefficients.

The fast Fourier transformation (FFT)-based spectral element method (SEM) was proposed by Doyle [18] and is very similar to the finite element method as far as the assembly and the solution of the equation of motion is concerned. Using the spectral element method, the general solution of the governing equations of motion, $\{u\} = (u_0(x, t), w(x, t), \phi(x, t), s(x, t))$, is represented by a spectral form as follows

$$\{u\} = \sum_{n=1}^{N} \{\hat{u}(x, \omega_n)\} e^{-j\omega_n t} = \sum_{n=1}^{N} \left(\sum_{m=1}^{M} \{\hat{u}^*_{mn}\} e^{-jk_{mn}x} \right) e^{-j\omega_n t} \tag{14}$$

where ω_n is the circular frequency at the nth sampling point and N is the frequency index corresponding to the Nyquist frequency in Fast Fourier Transform (FFT); k_{mn} is the mth wave number for the frequency ω_n. $\{\hat{u}\}$ represents the spectral amplitude vector corresponding to the generic displacement vector as a function of (x, ω_n) and $\{\hat{u}^*_{mn}\} = (\hat{u}_0, \hat{w}, \hat{\phi}, \hat{s})_{mn}$ represents the wave coefficient vector associated with the mth mode of wave and for each frequency, ω_n.

Substituting (14) into (6)–(9) the characteristic equation is obtained whose resolution will give the eight roots or wavenumbers k_{mn} for each value of the frequency ω_n which correspond to the different modes of the solution. Each wavenumber k_{mn} acts as a scale factor on the displacement variable in the same way that the frequency acts on the time.

Once the wavenumbers have been computed for each particular frequency ω_n the complex dynamic stiffness matrix is formed from the amplitude ratio matrix by using the force boundary conditions. The assembled system of spectral elements is solved at each sampling frequency. The time history of the field variables can then be post-processed using inverse FFT. More details about the derivation of the dynamic stiffness matrix can be found in [17].

The static formulation of the method is straightforward from the dynamic formulation by making the frequency tend to zero.

3. Element with embedded flexural crack

Intermediate crack-induced interfacial debonding is one of the most common debonding failure modes. It is widely accepted that debonding initiates at a major flexural crack and then propagates toward a plate end [6,23] (Fig. 1). High interfacial shear stresses at the vicinity of the flexural cracks originate this kind of failure mode.

A reliable and simplified non-expensive model is proposed in the present study based on the modification of the model of the previous section to incorporate IC debonding. Two different approaches might be considered to simulate the crack effects: the discrete and the smeared-crack approaches. The former treats cracking by adapting the geometry of the structure and keeping the interior of the body linear elastic, whereas the second approach keeps the geometry fixed and models the cracking process entirely via a constitutive law. Because of its simplicity, the smeared-crack approach has been widely used in spite of its mesh sensitivity. To overcome this, mathematical approaches such as the crack band model [24] have been proposed. However, this method is not capable of modelling individual macro-cracks because it tends to spread the crack formation over a region of the structure and its suitable use would require working with very small elements which involves huge computational cost.

On the other hand, in discrete crack modelling, unless the cracking path is known in advance, the mesh needs to be updated at each step to reflect the propagation of a crack, resulting in a complex process. In this work, a simplified discrete crack approach is employed to simulate the phenomena of the initialization and propagation of intermediate debonding for FRP sheet due to flexural cracks. The proposed model is formulated with the purpose of avoiding some of the disturbances derived from the use of crack approaches. In this way, a new spectral element with embedded crack is developed to replace the original element when a geometrical discontinuity appears. The nodes of the original element, which are used for the assembly with the rest of the element mesh, remain unaltered in the new element; in this way, the introduction of the new element causes few disturbances in the procedure. Furthermore, mesh bias is also avoided since the cracks are not defined along element boundaries.

In the absence of flexural crack or interfacial debonding, one spectral element such as was formulated in the previous section would be sufficient for analysis between any two nodes, 1 and 2. However, in the presence of an intermediate crack (Fig. 2a), the element should be reformulated to consider this effect. Fig. 2b shows schematically the spectral element model for an FRP-strengthened RC beam element with length L_e. With the appearance of crack the length of the element L_e is divided into three segments of lengths L_1, L_2 and L_3 in such a way that $L_e = L_1 + L_2 + L_3$ and the number of subelements increases from one to six. Crack is assumed to be at a distance of $L_1 + L_2/2$ from the node 1 and its height is h_1. The left and right segments (subelements 1 and 2) are treated as base-strengthened beams without crack and debonding while the intermediate section has been divided into four subelements to represent the crack effects: the through-height discontinuity between third and fourth subelements represents the flexural crack; meanwhile the materials above and below the crack (subelements 5 and 6) of heights h_2 and e_F, respectively, represent concrete and FRP, respectively. Nodes of the subelements 3 and 4 are located at the mid-height of the flexural crack.

In the same way, a length of debonding equal to L_2 has been assumed associated with the crack since the materials above and below debonding, i.e. concrete (subelements 3 and 4) and FRP (subelement 6), are treated as two beams separated out from the strengthened beam. This length might be assumed initially equal to the crack width and, subsequently, according to the evolution of the slip at the FRP–concrete interface might be expanded with the progressive debonding at the concrete–FRP interface.

The power of the proposed discrete crack model is due to its simplicity and possibility to be extended also in the case of other types of failure mode.

3.1. Kinematic relations

For the formulation of the new element we assume as previously that the cross-sectional interfaces between the base subelements (elements 1 and 2) and their adjacent elements in

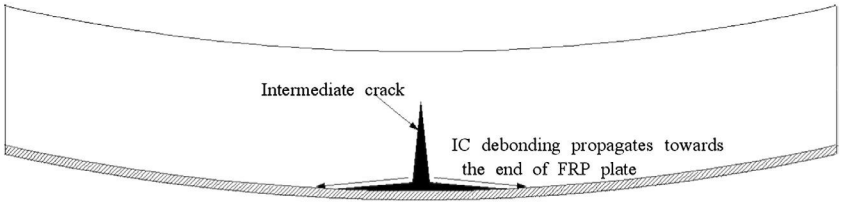

Fig. 1. IC debonding and its propagation.

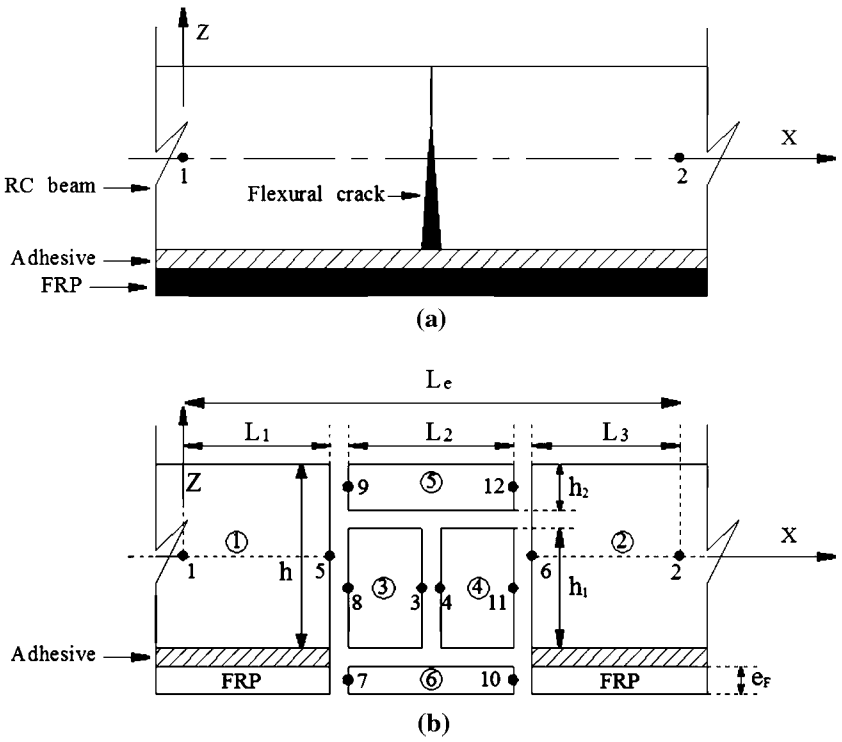

Fig. 2. (a) Two-node original element before the appearance of the flexural crack and location of the flexural crack; (b) reconfiguration of the element after the flexural crack.

Fig. 2b remain straight. Furthermore, the slope and the transverse displacement are continuous and constant at these interfaces. Under these assumptions, the following kinematic equations relating the nodal degrees of freedom at the left vertical interfaces can be obtained:

$$\{\hat{u}_7\}=\begin{pmatrix}\hat{u}_7^0\\ \hat{w}_7\\ \hat{\phi}_7\end{pmatrix}=\begin{pmatrix}\hat{u}_5^0+\left(\frac{h+e_F}{2}\right)\hat{\phi}_5+\hat{s}_5\\ \hat{w}_5\\ \hat{\phi}_5\end{pmatrix}=\begin{pmatrix}1 & 0 & \frac{h+e_F}{2} & 1\\ 0 & 1 & 0 & 0\\ 0 & 0 & 1 & 0\end{pmatrix}\begin{pmatrix}\hat{u}_5^0\\ \hat{w}_5\\ \hat{\phi}_5\\ \hat{s}_5\end{pmatrix}=[S_1]\{\hat{u}_5\} \tag{15}$$

$$\{\hat{u}_8\}=\begin{pmatrix}\hat{u}_8^0\\ \hat{w}_8\\ \hat{\phi}_8\end{pmatrix}=\begin{pmatrix}\hat{u}_5^0+\frac{h-h_1}{2}\hat{\phi}_5\\ \hat{w}_5\\ \hat{\phi}_5\end{pmatrix}=\begin{pmatrix}1 & 0 & \frac{h-h_1}{2} & 0\\ 0 & 1 & 0 & 0\\ 0 & 0 & 1 & 0\end{pmatrix}\begin{pmatrix}\hat{u}_5^0\\ \hat{w}_5\\ \hat{\phi}_5\\ \hat{s}_5\end{pmatrix}=[S_2]\{\hat{u}_5\} \tag{16}$$

$$\{\hat{u}_9\}=\begin{pmatrix}\hat{u}_9^0\\ \hat{w}_9\\ \hat{\phi}_9\end{pmatrix}=\begin{pmatrix}\hat{u}_5^0-\left(\frac{h-h_2}{2}\right)\hat{\phi}_5\\ \hat{w}_5\\ \hat{\phi}_5\end{pmatrix}=\begin{pmatrix}1 & 0 & -\frac{h-h_2}{2} & 0\\ 0 & 1 & 0 & 0\\ 0 & 0 & 1 & 0\end{pmatrix}\begin{pmatrix}\hat{u}_5^0\\ \hat{w}_5\\ \hat{\phi}_5\\ \hat{s}_5\end{pmatrix}=[S_3]\{\hat{u}_5\} \tag{17}$$

And similarly for the right vertical interfaces

$$\{\hat{u}_{10}\}=[S_1]\{\hat{u}_6\} \tag{18}$$

$$\{\hat{u}_{11}\}=[S_2]\{\hat{u}_6\} \tag{19}$$

$$\{\hat{u}_{12}\}=[S_3]\{\hat{u}_6\} \tag{20}$$

According to Eq. (14), the overhead hat indicates that the variables are discretized in the frequency domain. By using this reconfigured model, the displacements at the debonded area are assumed at the material level only, i.e. subelements 3, 4 (concrete) and 6 (FRP strip) retain their individualities throughout the analysis since the bond between them has disappeared adopting, therefore, a discrete layer model. Its adaptability to the general configuration of the strengthened beam is carried out with the relations (15)–(20) from which the displacements at the debonded area are mapped in terms of the displacements at the non-damaged areas (subelements 1 and 2).

3.2. Interfacial equilibrium

Fig. 3 shows the force balance at the interface between the base beam subelement 1 and the subelements 3, 5 and 6. From the equilibrium in this interface, the following equations are obtained

$$\begin{Bmatrix}\hat{N}_5\\ \hat{V}_5\\ \hat{M}_5\\ \hat{N}_5^*\end{Bmatrix}+\begin{Bmatrix}\hat{N}_7\\ \hat{V}_7\\ \hat{M}_7+\left(\frac{h+e_F}{2}\right)\hat{N}_7\\ 0\end{Bmatrix}+\begin{Bmatrix}\hat{N}_8\\ \hat{V}_8\\ \hat{M}_8+\frac{h-h_1}{2}\hat{N}_8\\ 0\end{Bmatrix}+\begin{Bmatrix}\hat{N}_9\\ \hat{V}_9\\ \hat{M}_9-\left(\frac{h-h_2}{2}\right)\hat{N}_9\\ 0\end{Bmatrix}+\begin{Bmatrix}0\\ 0\\ 0\\ \hat{N}_{5FRP}^*\end{Bmatrix}=0 \tag{21}$$

where N, V, M and N^* are the stress resultants associated with the variables u_0, w, ϕ and s, respectively.

Eq. (21) can be rewritten in matrix form as follows:

$$\{\hat{f}_5\}+[S_1]^t\{\hat{f}_7\}+[S_2]^t\{\hat{f}_8\}+[S_3]^t\{\hat{f}_9\}+\{\hat{f}_{5F}\}=0 \tag{22}$$

where $\{\hat{f}_{5F}\}$ indicates the force in the FRP plate correcting the imbalance between the base subelement 1 and the sixth subelement.

Similarly, the equilibrium at the interface between subelement 2 and subelements 4, 5 and 6 can be written as

$$\{\hat{f}_6\}+[S_1]^t\{\hat{f}_{10}\}+[S_2]^t\{\hat{f}_{11}\}+[S_3]^t\{\hat{f}_{12}\}+\{\hat{f}_{6F}\}=0 \tag{23}$$

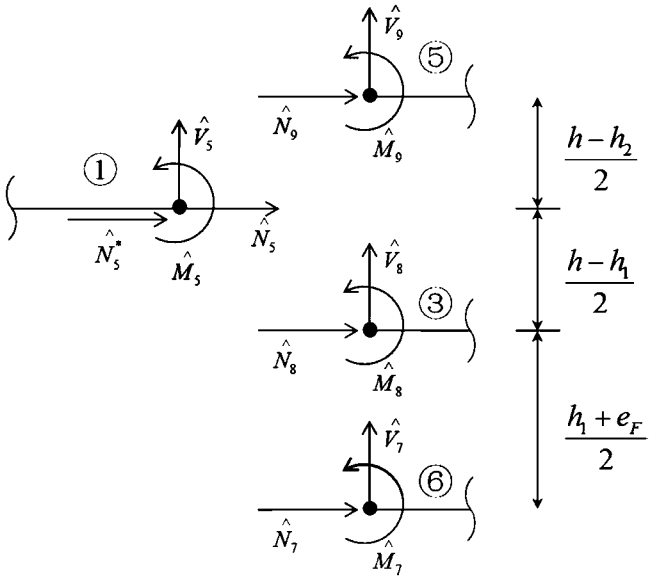

Fig. 3. Force balance.

At the crack surface between the third and the fourth subelements, we have

$$\{\hat{f}_3\} + \{\hat{f}_4\} = 0 \tag{24}$$

However, under the assumption of no contact between the surfaces adjacent to the crack, we get

$$\begin{aligned} \{\hat{f}_3\} &= 0 \\ \{\hat{f}_4\} &= 0 \end{aligned} \tag{25}$$

3.3. Assembly

In a general way, the equilibrium equation for each one of the six subelements j ($j = 1,\ldots,6$) with nodes p and q can be expressed using submatrices of the stiffness matrix as

$$\begin{pmatrix} [\hat{K}^j_{11}] & [\hat{K}^j_{12}] \\ [\hat{K}^j_{21}] & [\hat{K}^j_{22}] \end{pmatrix} \begin{pmatrix} \{\hat{u}_p\} \\ \{\hat{u}_q\} \end{pmatrix} = \begin{pmatrix} \{\hat{f}_p\} \\ \{\hat{f}_q\} \end{pmatrix} \tag{26}$$

where the stiffness submatrices $\hat{K}^n_{ij}$ can be calculated by employing the spectral element method presented in the previous section including FRP or not depending on the subelement.

By taking the kinematic relations and equilibrium nodal forces of the six internal subelements presented above, subsequently the assembled matrix of the flexural crack spectral element can be obtained as:

$$\begin{bmatrix} K_{11} & 0 & 0 & 0 & K_{15} & 0 \\ 0 & K_{22} & 0 & 0 & 0 & K_{26} \\ 0 & 0 & K_{33} & 0 & K_{35} & 0 \\ 0 & 0 & 0 & K_{44} & 0 & K_{46} \\ K_{51} & 0 & K_{53} & 0 & K_{55} & K_{56} \\ 0 & K_{62} & 0 & K_{64} & K_{65} & K_{66} \end{bmatrix} \begin{Bmatrix} \hat{u}_1 \\ \hat{u}_2 \\ \hat{u}_3 \\ \hat{u}_4 \\ \hat{u}_5 \\ \hat{u}_6 \end{Bmatrix} = \begin{Bmatrix} \hat{f}_1 \\ \hat{f}_2 \\ 0 \\ 0 \\ 0 \\ 0 \end{Bmatrix} \tag{27}$$

By condensing out the degrees of freedom at the interfaces (nodes 3, 4, 5 and 6) the system (27) might be reduced to

$$\begin{bmatrix} K^*_{11} & K^*_{12} \\ K^*_{21} & K^*_{22} \end{bmatrix} \begin{pmatrix} \{\hat{u}_1\} \\ \{\hat{u}_2\} \end{pmatrix} = \begin{Bmatrix} \hat{f}_1 \\ \hat{f}_2 \end{Bmatrix} \tag{28}$$

where

$$K^*_{11} = K_{11} + K_{15} r_{51} \tag{29}$$

$$K^*_{12} = K_{15} r_{52} \tag{30}$$

$$K^*_{21} = K_{26}(r_{65} r_{51} + r_{61}) \tag{31}$$

$$K^*_{22} = K_{22} + K_{26} r_{65} r_{52} \tag{32}$$

$$r_{51} = R^{-1}\left(K_{64} K_{44}^{-1} K_{46} - K_{66}\right) r_{61} \tag{33}$$

$$r_{52} = -R^{-1} K_{62} \tag{34}$$

$$R = K_{66} r_{65} - K_{64} K_{44}^{-1} K_{46} r_{65} + K_{65} \tag{35}$$

$$r_{65} = K_{56}^{-1}\left(K_{53} K_{33}^{-1} K_{35} - K_{55}\right) \tag{36}$$

$$r_{61} = -K_{56}^{-1} K_{51} \tag{37}$$

Therefore, with the appearance of flexural crack the usual spectral element is replaced with this new spectral element by employing the reconstructed stiffness matrix. The original nodes, 1 and 2, remain unaltered with respect to the original mesh configuration, removing any perturbation in the global mesh configuration when this element is inserted.

4. Material models

Stiffness coefficients in Eqs. (6)–(13) are computed using a layer discretization of the cross-section as follows

$$\begin{aligned} [A_{11} \quad B_{11} \quad D_{11}] = \sum_{i=1}^{NCC} \int_{z_{1Ci}}^{z_{2Ci}} \tilde{E}_{Ci} [1 \quad z \quad z^2] b_C dz \\ + \int_{z_{1F}}^{z_{2F}} E_F [1 \quad z \quad z^2] b_F dz + \sum_{j=1}^{NSS} \tilde{E}_{sj} A_{sj} [1 \quad z_j \quad z_j^2] \end{aligned} \tag{38}$$

$$[A_{22}] = \sum_{i=1}^{NCC} \int_{z_{1Ci}}^{z_{2Ci}} \tilde{G}_{Ci} b_C dz + \int_{z_{1F}}^{z_{2F}} G_F b_F dz \tag{39}$$

$$[A_F \quad B_F] = \int_{z_{1F}}^{z_{2F}} E_F [1 \quad z] b_F dz \tag{40}$$

where the concrete section has been divided into NCC strips, each one limited by z_{1Ci} and z_{2Ci}, to model the progressive cracking and crushing of the material through the beam height. For concrete and steel, the tangent moduli are replaced by the equivalent secant elastic moduli, $\tilde{E}_C(\varepsilon_{xC})$, $\tilde{G}_C(\gamma_{x\ zC})$, $\tilde{E}_S(\varepsilon_{xS})$ and $\tilde{G}_{AD}(\gamma_{xz\ AD})$ since, due to the material nonlinearity, the elastic modulus is not constant but is a function of the strain at every point.

The stress–strain behaviour of each layer is described through a one-dimensional nonlinear constitutive model for the corresponding material. Realistic nonlinear constitutive models should be employed to represent the stress–strain behaviour of concrete, reinforcing steel and bonded FRP of each of the layers in which the cross-section are discretized.

4.1. Concrete

The model specified in the CEB-FIP Model Code [25] is used to describe the nonlinear stress–strain relationship for the concrete. Compressive concrete behaviour is represented by a parabolic curve as follows

$$\frac{\sigma_c}{f_{cm}} = -\left(\frac{k\eta - \eta^2}{1 + (k-2)\eta}\right) \tag{41}$$

where

$$\eta = \frac{\varepsilon_c}{\varepsilon_{c1}} \qquad k = \frac{E_c}{E_{c1}} \tag{42}$$

and where f_{cm} is the compressive strength of concrete, which is taken to be the cylinder compressive strength in this study, ε_{c1} is the strain at maximum compressive stress. E_c and E_{c1} denote the elastic modulus and the secant modulus from the origin to the peak compressive stress, respectively.

For concrete under uniaxial tension, from zero to maximum tensile strength point ($\varepsilon_{ctm}, f_{ctm}$), a linear elastic behaviour has been assumed with a slope equal to the initial compression Young's modulus. For a cracked section, the tension softening bilinear approach proposed in [25] has been adopted in this study

$$\sigma_{ct} = f_{ctm}\left(1 - 0.8\frac{w}{w_1}\right) \quad \text{for} \quad w \le w_1 \tag{43}$$

$$\sigma_{ct} = f_{ctm}\left(0.25 - 0.05\frac{w}{w_1}\right) \quad \text{for} \quad w_1 \le w \le w_c \tag{44}$$

where w is the crack opening in mm, $w_1 = G_F/f_{ctm}$ in mm, $w_c = 5{\cdot}G_F/f_{ctm}$ in mm, G_F is the fracture energy in N/mm given by

$$G_F = 73 f_{cm}^{0.18} \tag{45}$$

and f_{ctm} is the tensile strength in MPa given by

$$f_{ctm} = 0.3(f_{cm} - 8)^{23} \tag{46}$$

4.2. Steel and FRP bond behaviour

For the steel rebars a bilinear isotropic-hardening stress–strain law has been adopted. Although a bond–slip relation is assumed for the FRP/concrete interface, as described below, full bond is assumed between the concrete and steel reinforcement.

The FRP reinforcement is modelled with elastic–brittle behaviour in tension and zero strength and stiffness in compression. The failure strain in tension is obtained as the minimum between the material rupture strain and the debonding strain, computed using an appropriate debonding model. IC debonding is a common failure mode in FRP plates/sheets strengthening of RC elements in flexure. An accurate description of slip concentrations near a localised flexural crack is important for accurate predictions of IC debonding failures. In the literature, many semi-empirical models exist that describe and evaluate debonding stresses of FRP plates/sheets externally bonded to a concrete surface [9,26]. Here, it is assumed that IC debonding depends only on the bond–slip behaviour parallel to the FRP–concrete bonded interface since previous studies [27,28] have shown that the interfacial normal stress at the FRP–concrete interface is insignificant away from the plate ends and, therefore, has no influence on the IC debonding failure mode.

A bond–slip model will be used to study the debonding phenomenon between FRP and concrete. Although this model is assigned to the adhesive interface, non-linear behaviour of adhesive and concrete cover affecting the debonding failure mode are really included in the interface law, i.e. nonlinearities of concrete cover at high shear stress levels are taken into account at the slip model. Several shear bond–slip constitutive relations have been proposed to simulate the behaviour at the concrete–FRP interface. An interesting review of some of these models was presented in [26]. They were assessed on 253 pull tests carried out on FRP-to-concrete bonded joints, leading to a conclusion that a more precise model is required. In this work, the simplified bond–slip model for FRP externally bonded to concrete proposed by Lu et al. [26] has been used. This model was developed from the predictions of a meso-scale finite element model and its constitutive relations are as follows (Fig. 4)

$$\tau = \tau_{\max}\sqrt{\frac{s}{s_0}} \qquad \text{if } s < s_0 \tag{47}$$

$$\tau = \tau_{\max} e^{-\alpha\left(\frac{s}{s_0} - 1\right)} \qquad \text{if } s \geqslant s_0 \tag{48}$$

$$s_o = 0.0195\beta_w f_{ctm}, \quad \tau_{\max} = \alpha_1 \beta_w f_{ctm}, \quad \alpha_1 = 1.5 \tag{49}$$

$$\beta_w = \sqrt{\frac{2 - b_F/b_c}{1 + b_F/b_c}} \tag{50}$$

$$\alpha = \frac{1}{\frac{G_f}{\tau_{\max} s_0} - \frac{2}{3}}, \quad G_f = 0.308\beta_w^2\sqrt{f_{ctm}} \tag{51}$$

This model has first an ascending branch (Eq. (47)) delimited by a bond shear stress $\tau_{\max}$ and a slip s_0, and a subsequent exponential softening branch (Eq. (48)) whose shape is controlled by the parameter α, which is related to interfacial fracture energy G_f. The bond–slip curve is assumed to unload linearly through the origin when the interface is in the softening range. The parameters defining the constitutive law are obtained from the concrete tensile strength f_{ctm}, which can be obtained from the compressive strength of concrete f_{cm}, the interfacial fracture energy G_f and the width ratio factor β_w, depending on the width of concrete beam b_c and FRP strip b_F. The value of f_{ctm} has been taken from Eq. (46).

5. Crack pattern

The crack pattern along the FRP-strengthened RC beam has a major influence on its structural performance, including the failure mechanism. Therefore, in the proposed element in Section 3, the height, location and spacing of flexural cracks play an important role for the success of the simulation. The height, which allows following the crack evolution, can be defined through a fibre analysis of the concrete cross section such as introduced in the previous section. The appearance of crack, i.e. crack location, is based on the concrete tensile constitutive law. Once a section of the element has cracked, length $L_1 + L_2/2$ in Fig. 2b is defined. In the proposed approach, only one crack is allowed per element, which means that crack spacing acts as a constraint to specify the element size,

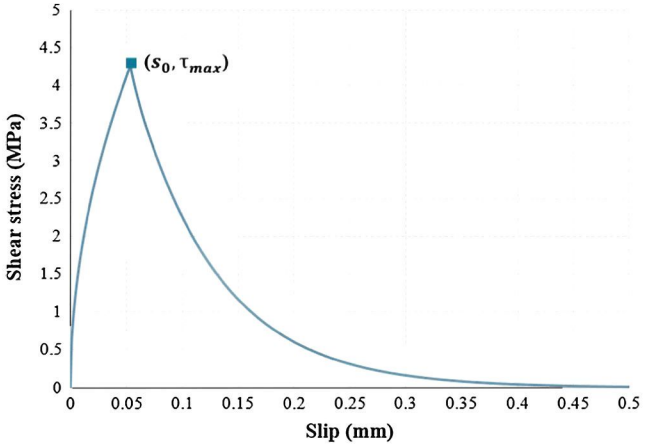

Fig. 4. Lu's bond–slip model.

especially in the cracked areas. Moreover, the evaluation of mean crack spacing has a great effect on the shear stress transfer between the concrete and the FRP strip.

Although some expressions have been proposed in the literature to define the crack spacing in RC beams, no effective approach has been developed to evaluate the mean crack spacing of an FRP-strengthened RC beam.

An expression is reported in the actual European design guide [29] based on the modification of the unstrengthened beam crack spacing with a factor accounting for an homogenised reinforcing area, comprehensive of the internal steel rebars and the external FRP plate. Following this approach, the proposed mean crack spacing L_{cm} is computed in [30] making use of the CEB Bulletin 203–205 [31] formulation as follows

$$L_{cm} = \frac{\Phi}{3.6\rho_{sl,eff}}\frac{1}{\omega} \tag{52}$$

where Φ is the diameter of reinforcing steel bar and $\rho_{sl,eff}$ is the steel reinforcement ratio to the effective area of concrete in tension, which can be obtained in the following way

$$A_{C,eff} = \min\left\{2.5cb, \frac{b(h-y)}{2}\right\} \tag{53}$$

where y is the height of the compression zone of the beam section, c is the concrete cover, b and h are the width and the height of the beam, respectively.

The homogenisation coefficient ω can be obtained as

$$\omega = \frac{n_s\rho_{sl,eff} + n_F\rho_{Fl,eff}}{n_s\rho_{sl,eff}} \tag{54}$$

where n_s and n_F are the homogenisation coefficients of the steel and FRP reinforcements, respectively, and $\rho_{Fl,eff}$ is the FRP reinforcement ratio to the effective area of concrete in tension.

In [30] two other formulations have been employed to evaluate the crack spacing. The first is based on the introduction of Eq. (54) in the crack spacing expression given by the CEB Bulletin 235 [32] and the second one is due to the extension given by Beeby [33] of the crack spacing formulation reported by the Eurocode 2 [34].

However, in a comparison of the three approaches of computing L_{cm} performed on 130 experimental tests [30], a better correlation of the predicted failure loads with the experimental values was obtained by using Eq. (52). Therefore, element sizes in the cracked area will be defined with this reference formulation.

6. Post-debonding behaviour

The proposed approach will be able to predict the ultimate load for which FRP debonding occurs. The post-debonding behaviour might only be captured by using a displacement control strategy and the arc-length method, which can give convergence difficulties. However, the prediction of residual strength of an FRP-strengthened RC beam might be necessary to evaluate the safety of the beam when debonding happens.

A simple methodology has been adopted in this study to predict post-debonding strength without carrying out complex stress or fracture analyses. As it is known, debonding and associated fracture processes cause global energy transformations in FRP-strengthened members. Furthermore, the amount of energy dissipated in the system during debonding can be determined from the difference between the recoverable energy stored in the beam before and after debonding. In [35], the total dissipation in the system provided by the debonding phenomenon is calculated from the load–deflection curves as follows

$$\Delta D = \frac{P_{2d}^2}{2K_2} - \frac{P_{1d}^2}{2K_1} \geqslant 0 \tag{55}$$

where P_{2d} and P_{1d} represent the load values before and after FRP debonding, respectively. K_2 and K_1 are the stiffness values for the strengthened and unstrengthened beams, respectively, and are given by

$$K_2 = 2EI_2 \Big/ \left[\frac{l_s^2 L}{2} - \frac{2l_s^3}{3}\right], \quad K_1 = 2EI_1 \Big/ \left[\frac{l_s^2 L}{2} - \frac{2l_s^3}{3}\right] \tag{56}$$

where I_1 and I_2 are the moments of inertia of the transformed beam sections in cracked condition, L is the beam length and l_s is the shear span.

From Eq. (55), the upper limit of residual strength of FRP-strengthened RC beam can be estimated in an approximate way as follows

$$P_{1d} \leq P_{2d}\sqrt{\frac{K_1}{K_2}} \tag{57}$$

7. Validation of the proposed model

7.1. Implementation of the model

Implementation of the developed model was performed to compare the model predictions with some experimental results.

While the tensile stresses in the concrete are below its tensile strength and the stresses in the steel rebars have not reached the elastic limit, the calculation procedure is elastic and the stiffness coefficients in Eqs. (38)–(40) are valid considering that the initial tangent elastic moduli of the concrete and reinforcement steel are applicable to all the concrete section and all the steel rebars, respectively. The same is applicable to the adhesive. However, when applied load increases and nonlinear behaviour of materials begins, the elastic modulus is not constant but is a function of the strain at every point. This phenomenon is introduced by using equivalent secant elastic moduli for the concrete, the steel reinforcement and the adhesive instead of the initial tangent elastic moduli when it corresponds. The behaviour of the FRP keeps linear elastic up to failure.

Through the division of the concrete section into fibres, the progressive cracking of the section is modelled. When nonlinear phenomena develop, the stiffness coefficients are functions of the unknown displacements. Since this relation cannot be established explicitly but implicitly in a nonlinear way, a linearised iterative secant procedure at different load levels has been used to achieve the solution.

The developed FRP debonding with embedded flexural crack model can be easily integrated into the model of FRP-strengthened beams to predict their behaviour in the case of IC FRP debonding failure. To do so, firstly, the mean crack spacing L_{cm} defined in Eq. (52) will be taken as a reference to define the size of the elements, at least at the cracked portion of the beam. When flexural cracking appears, the proposed discrete crack element will replace the usual element to simulate the behaviour of the cracked area. Initially, a sufficiently small size of the cracked area (L_2 in Fig. 2b) should be chosen. As the load increases, the slip value is checked at nodes 5 and 6 (Fig. 2b) with the purpose of verifying if interfacial debonding progresses or not. FRP debonding will expand as soon as slip at the checked nodes reaches the maximum slip value, i.e. the value for which the interfacial shear stress is zero, defined according to the constitutive law defined for the concrete–FRP interface. Then, the length L_2 in Fig. 2b will be broadened and the procedure of checking the slip value for the new locations of nodes 5 and 6 will be repeated again. Usually, when slip at nodes 5 and 6 reaches the maximum value the debonding propagates suddenly along the whole element and nodes 5 and 6 in Fig. 2b

merge with nodes 1 and 2, respectively, which means that the whole elements has debonded. The numerical procedure is summarised in the flowchart shown in Fig. 5.

7.2. Correlation between numerical simulation and experimental results

To evaluate the accuracy of the proposed numerical model for IC debonding, the results from three FRP-plated beams experimentally tested in [21] were used. These specimens were chosen for comparison because their failure was initiated by midspan debonding and, furthermore, the necessary data of these beams to be used in the model were available. Using the proposed approach, the load–deflection behaviour as well as the distribution of interface stresses of strengthened beams may be obtained.

Seven FRP-strengthened RC beams (BF2-BF6, BF8 and BF9) and two unstrengthened RC beams (BF1 and BF7) were tested by Matthys [21]. BF4, BF5 and BF6 were precracked, preloaded and anchored, respectively, and were not used in this study. All specimens were strengthened by one layer FRP except BF9 which was covered by two layers of FRP in the lower face of the RC beam. Specimens BF2 and BF8 were chosen in this work to validate the proposed approach. Geometrical and material properties of the chosen specimens as well as loading configuration are listed in Table 1 and Fig. 6.

For a uniform beam domain not containing any discontinuity in terms of geometry, material or external load, one single spectral element should be enough to simulate its behaviour. For our study, in order to predict the failure of the strengthened beam and, therefore, its progressive degradation, more elements would be necessary. Only one element was used for the portion of the non-strengthened beam close to the support considering its uniformity and that cracking phenomenon will not occur in that area. To define the element size in the strengthened beam, the value of the mean crack spacing, 100 mm, calculated according to Eq. (52) was used, giving as a result a mesh of 19 elements in the strengthened portion, considering that only half of the specimen was modelled by taking advantage of symmetry, plus one element in the unstrengthened portion. The size of the elements might even be increased in those areas of the strengthened portion close to the FRP plate ends in which cracking will not occur. Compared with the conventional FE models, in the proposed approach the number of elements has been reduced drastically from tens of thousands to a few tens in numerical simulation, which means a huge saving in computational cost.

Figs. 7 and 8 illustrate the comparison of the spectral model prediction of the load–deflection response for the FRP-strengthened beams BF2 and BF8, respectively, along with the experimental results. The results show that the predicted ultimate loads of the two specimens agree well with the experimental data. Furthermore, the successive stages of the strengthened beam under increasing load, from the uncracked state to the cracked state, followed by yielding of the internal steel reinforcement, are predicted in an acceptable way by the model considering its simplicity and the high number of parameters involved in the behaviour of these types of structures. Predictions obtained in [9] with a refined FE model are also shown. In Chen et al's model [9], 11,014 finite elements were used and, furthermore, the bond behaviour between concrete and internal steel reinforcement has been simulated. Chen et al's model might be taken as a reference taking into account its accuracy when compared with experimental results. However, the accuracy of the proposed model can be considered very good considering that a mesh of only 20 elements was used. In addition, by using the procedure shown in Section 6, the post-debonding behaviour of the beam is also captured reasonably in a very simple way if it is compared with the predictions obtained with the reference model. There are no experimental predictions for this behaviour since displacement control was not used in the laboratory tests. However, numerical predictions and experimental results for reference unstrengthened beams BF1 and BF7 are also shown in Figs. 7 and 8, respectively. For these unstrengthened specimens the agreement between experimental and numerical results is also good. Furthermore, these results are also suitable to validate the post-debonding model used in the strengthened beams.

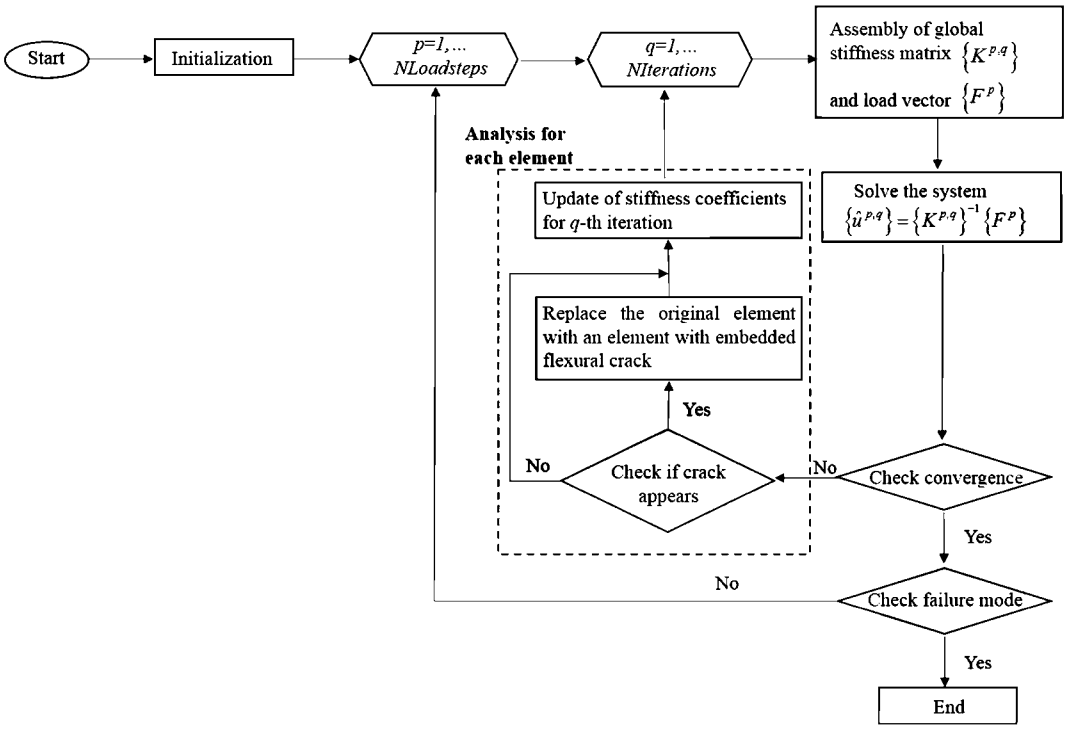

Fig. 5. Implementation of the numerical model.

Table 1
Material and geometrical properties of selected specimens for numerical simulation.

	Specimens	BF2	BF8
RC beam	Span (mm)	3800	3800
	Width b_c (mm)	200	200
	Height h_c (mm)	450	450
Concrete	Elastic modulus E_c (MPa)	28,580	29,690
	Compressive strength f_c' (MPa)	36.5	39.4
	Tensile strength f_t (MPa)	2.814	3.002
Internal steel reinforcement	Tension bars/yield strength f_{yt} (MPa)	4Y16/590	2Y16/590
	Compression bars/yield strength f_{ct} (MPa)	2Y16/590	2Y16/590
	Elastic modulus E_s (GPa)	200	
CFRP reinforcement	Thickness (mm)	1.2	
	Width (mm)	100	
	Length (mm)	3660	
	Elastic modulus E_F (GPa)	159	
	Tensile strength f_F (MPa)	3200	

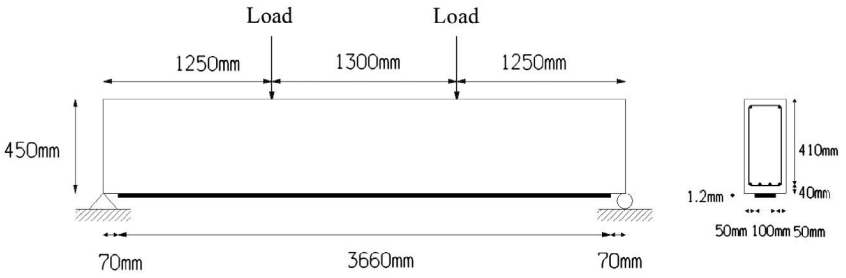

Fig. 6. Four-point bending test.

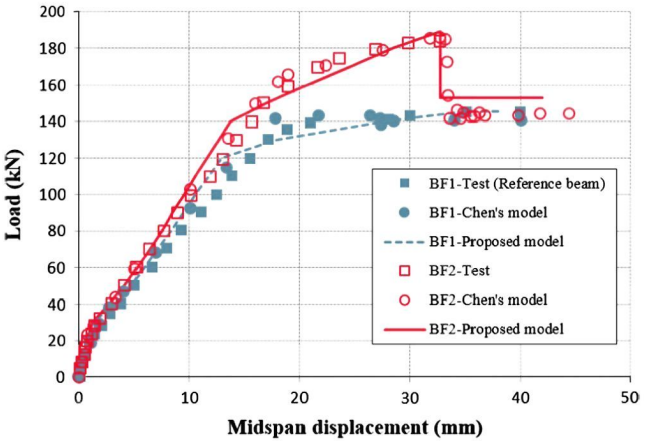

Fig. 7. Load–displacement comparison for specimens BF1 and BF2.

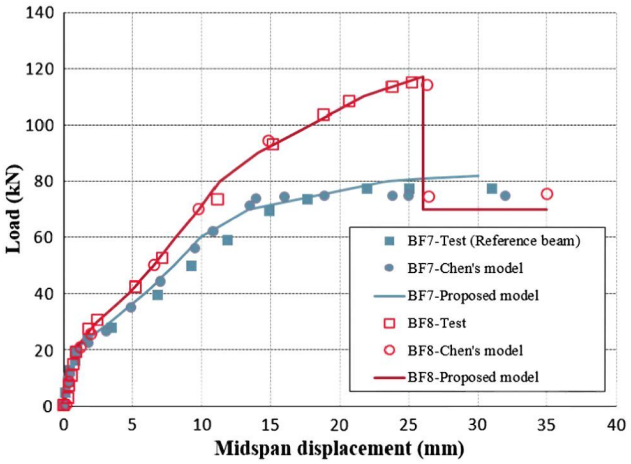

Fig. 8. Load–displacement comparison for specimens BF7 and BF8.

The local behaviour at the adhesive–concrete interface considering flexural cracking of the RC beam is shown in Figs. 9 and 10 for beams BF2 and BF8, respectively, at the onset of debonding by using the FRP strain profile. The strain in the FRP is a maximum at the crack positions as the tensile strain is resisted solely by the FRP. The strain in the FRP between the cracks decreases as both the FRP and concrete resist the tensile strains. Comparisons were made with the post-cracking experimental results obtained for the specimen BF2, which were available in [21], and with the numerical predictions under ultimate load carried out in [9] for BF2 and BF8. Experimental values are shown in the figure only for a limited number of points corresponding to the location of the strain gauges used during the test. The experimental test maximum strain values for both specimens are also shown. As expected, there is a strong increase in the strain at failure at the loading points characteristic of the interfacial debonding at the more loaded region. The debonded regions can be identified as the regions of constant FRP strain. In general, the predicted values of the maximum longitudinal strain in the FRP plate at debonding failure between the two concentrated loads are in good agreement with the experimental strain values used for comparison, considering the simplicity of the model used. However, for more external regions it is clear that the data predicted in [9] are higher than the predicted data with the proposed model. The main reason for this disagreement is due to the fact that this model is not able to simulate shear cracks which occur especially at the shear span; only flexural cracks are simulated which are predominant in the region between the two loads. For this reason, more accurate predictions are obtained where the strains are higher in spite of the simplicity of the model. To demonstrate this, predictions obtained for specimen BF2, when subjected to a lower load level of 70 kN are compared

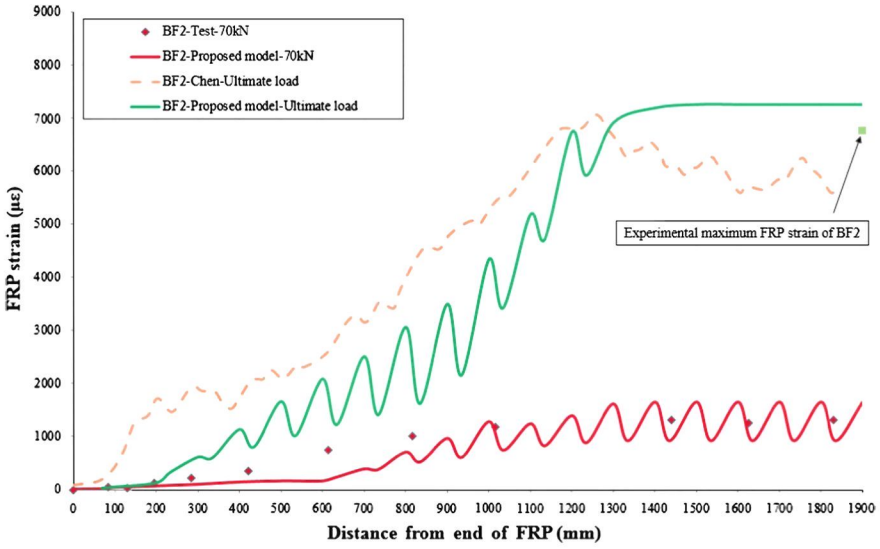

Fig. 9. FRP strain profile of specimen BF2.

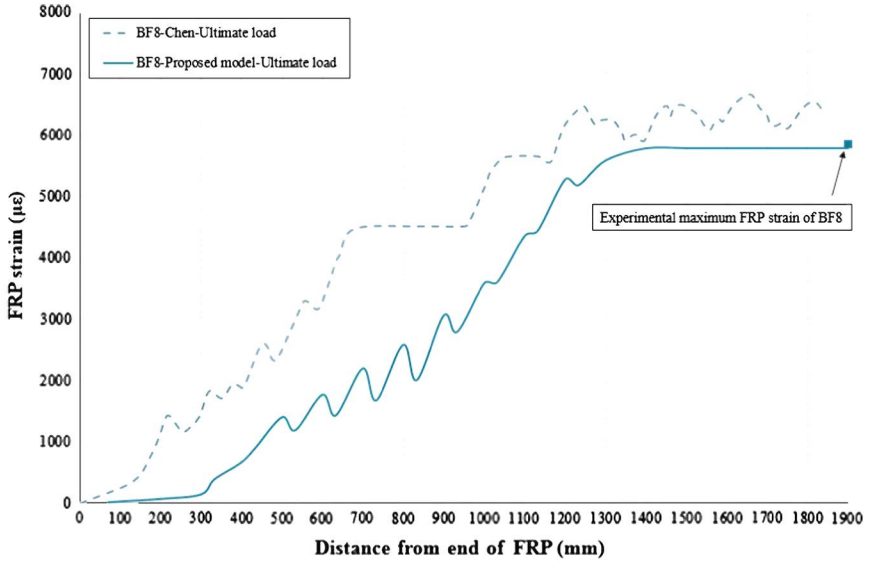

Fig. 10. FRP strain profile of specimen BF8.

with experimental results. In this case, the agreement at the shear span is much better since the effect of shear cracks decreases remarkably due to the low load level.

The shear stress at the concrete–FRP interface is another key factor to analyse the local behaviour under the ultimate load of the strengthened beam since the debonded regions can also be identified as the regions of zero shear stress. Its distribution is strongly dependent on the chosen bond slip model. Figs. 11 and 12 show the bond shear stress along the length of the concrete–FRP interface for specimens BF2 and BF8 at the onset of debonding. The bond stress is zero between the two loading points which means localised debonding. Areas close to the zero bond stress region indicate that the interfacial stress state is at the descending branch of the bond–slip model. All other stresses beyond this area are in the ascending branch. In fact, a peak shear stress point appears in the vicinity of the concentrated load at the more external region. The presence in this area of fluctuating interfacial shear stress values are consequence of the sudden slip due to the appearance of cracks. The same phenomenon was observed in [9,12]. The interfacial shear stress distribution suggests that failure is initiated in the pure bending zone and then suddenly propagated towards the plate ends. Thus, this demonstrates that intermediate debonding is the predominant failure mode originated in the region of flexural cracking.

For BF2 specimen, bond shear stress distributions before cracking (15 kN) and after cracking (70 kN) are also shown in Figs. 13 and 14, respectively. In the same way, the evolution of the mesh used for the half of the beam for these two level loads as well as 184 kN (onset of debonding) is shown in Fig. 15. At the initial stages, before cracking, practically interfacial shear stresses do not appear since the values are very low. As expected, only when cracks appear bond shear stresses increase in the cracked areas.

8. Dynamic study

One of the main advantages of the proposed model is its ability to be applied also to solve dynamic problems and calculate modal parameters of the strengthened structure, including high

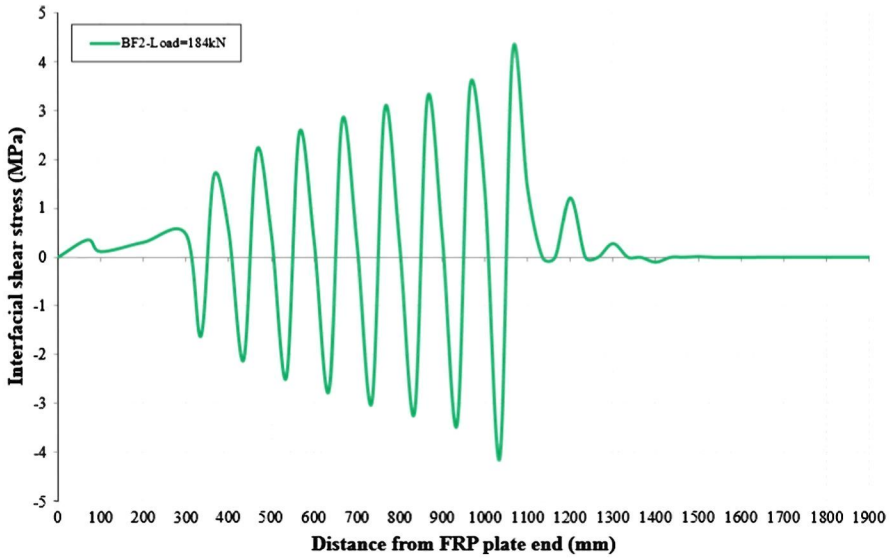

Fig. 11. Bond shear stress distribution predicted for BF2 at the onset of debonding (184 kN).

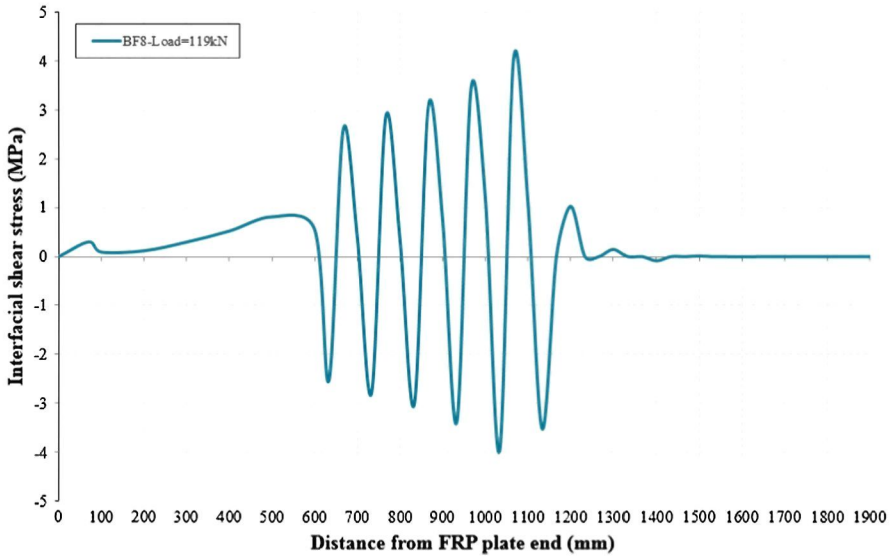

Fig. 12. Bond shear stress distribution predicted for BF8 at the onset of debonding (119 kN).

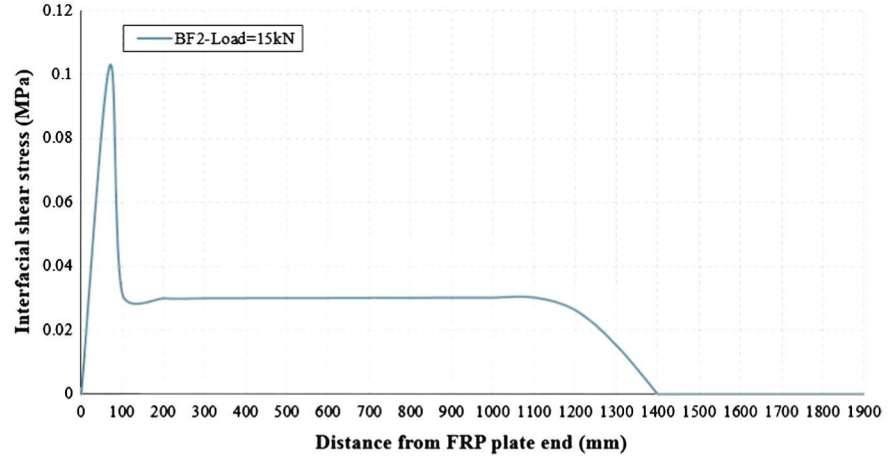

Fig. 13. Bond shear stress distribution predicted for BF2 before cracking (15 kN).

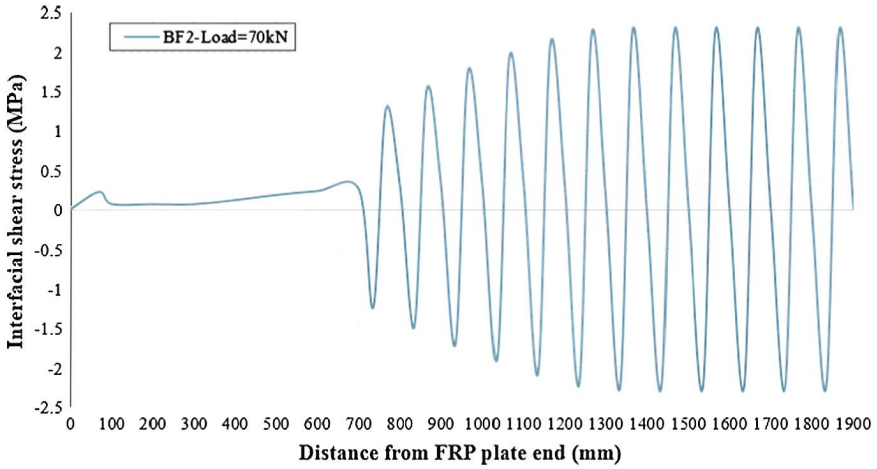

Fig. 14. Bond shear stress distribution predicted for BF2 after cracking (70 kN).

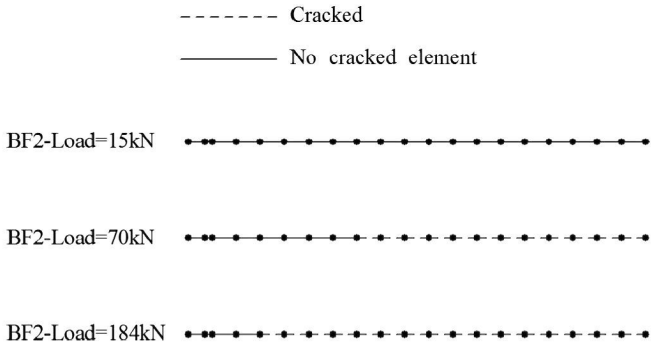

Fig. 15. Spectral element mesh evolution for BF2 under different loading stages.

frequency problems. It is highly interesting to examine the dynamic behaviour of these kinds of FRP-strengthened beams when an IC debonding mechanism occurs. Furthermore, it would be very useful to study the response of these beams under high rate loads and as a tool to detect the initiation of interfacial debonding since, in that case, only high frequencies are expected to undergo changes. With this purpose, a numerical dynamic study based on modal frequencies is carried out here to check the behaviour of the strengthened beam when flexural cracks and debonding originate.

Specimen BF2 from the previous section has been used in this study. It was subjected to a vertical chirp input of low amplitude in the frequency range of 0–2 kHz applied near the midspan section. Firstly, different scenarios of flexural cracking were considered by varying the location and the depth of predefined cracks. Unlike the smeared-crack models, location and depth of the crack and its influence on the dynamic behaviour of the structure can be perfectly simulated. For each condition, the vertical response signal was captured in six equally spaced points which might be assumed to measurement channels, using a sampling frequency of 2 Hz. Although the problem might have been simulated with only one element of the proposed model predefining the geometrical characteristics of the crack, more elements were considered with the purpose of making nodes of the model coincident with the load location and the output channels. The spectra obtained for each channel were combined into the average normalised power spectral density (ANPSD), which is shown for different conditions in Fig. 16. In the same way, Table 2 shows the captured frequencies for the different damage scenarios. As expected, the decrease in frequencies with the appearance of cracks is reflected by the proposed model; the higher the crack depth, the higher the rate that occurs. Furthermore, due to the local nature of the phenomenon the changes are more evident for the higher frequencies.

In a second part of this study, the influence of the length of debonding (L_2 in Fig. 2b) is explored. To do this, by predefining a

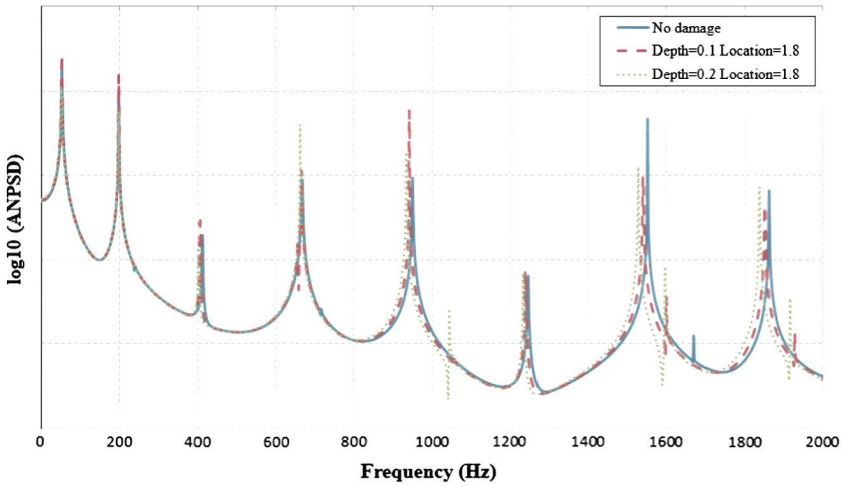

Fig. 16. ANPSD for different crack conditions.

Table 2
Variation of modal frequencies for flexural cracking.

Relative crack depth	No crack	0.1 m		0.2 m	
Relative crack location (from left support)		0.6	1.8	0.6	1.8
f_1 (Hz)	52.15	52.15	52.12	52.11	50.15
f_2 (Hz)	198.28	196.21	198.28	196.24	195.28
f_3 (Hz)	412.49	406.49	406.49	402.48	402.48
f_4 (Hz)	667.53	660.75	664.38	662.73	662.73
f_5 (Hz)	949.01	943.13	940.99	939.05	932.98
f_6 (Hz)	1247.28	1241.26	1239.22	1235.27	1233.26
f_7 (Hz)	1551.57	1543.37	1539.51	1535.56	1527.55
f_8 (Hz)	1861.87	1849.86	1849.86	1831.81	1837.85

Table 3
Variation of modal frequencies with the length of debonding. Flexural crack height = 0.1 m; location = 0.6 m.

Frequencies	No crack	Length of debonding (mm)		
		0.95	1.9	4.75
f_1 (Hz)	52.15	52.15	52.15	52.15
f_2 (Hz)	198.28	198.28	198.28	198.28
f_3 (Hz)	412.49	411.60	411.58	410.49
f_4 (Hz)	667.53	666.65	666.62	664.73
f_5 (Hz)	949.01	949.12	949.01	949.01
f_6 (Hz)	1247.28	1246.58	1246.26	1245.28
f_7 (Hz)	1551.57	1551.61	1550.85	1549.57
f_8 (Hz)	1861.87	1860.38	1860.35	1857.86
...	...	...	...	...
...	...	...	...	...
f_{68} (Hz)	14267.75	14266.41	14264.15	14261.57
f_{69} (Hz)	14564.06	14561.63	14559.37	14552.26
f_{70} (Hz)	14859.35	14856.73	14854.31	14848.42

crack height of 10 cm, spectra for values of L_2 equal to 0.95, 1.9 and 4.75 mm were obtained by using the same previous procedure as for flexural cracks. The differences among the different lengths are very small, which means that the possible variations in frequencies will be of a very local nature. For this reason, a frequency range between 0 and 15 kHz was used in this second study. The same model as in the previous example was used. Table 3 shows the predictions of modal frequencies for the analysed cases. The first frequencies and the closest frequencies to 15 kHz are shown. As expected, lower frequencies do not undergo changes with debonding. However, for higher natural frequencies, close to 15 kHz, changes due to debonding appearing become detectable, even considering that a very small length of debonding is assumed. These changes would become more noticeable if frequencies higher than 15 kHz were considered; their detection would be very useful as a tool to identify minor defects before their broadening with the purpose of preventing future failures which might be catastrophic. This application demonstrates the importance of having a methodology able to work in the high frequency range without time consuming numerical computation, as would occur if the finite element method were used. This is one of the main achievements of the proposed method which is able to solve both static and dynamic problems, even those in the high frequency range without additional cost, in a very simplified way. Furthermore the defects are considered in a discrete way which better coincides with the physical reality of the problem.

9. Conclusions

A new discrete crack approach has been presented in this paper for the numerical prediction of IC debonding failures in FRP-strengthened RC beams. The following conclusions are drawn from the results of the study:

- The new approach overcomes the major deficiency of all existing refined finite element models related to cost and complexity.
- The new model has been developed in a simple and non-expensive 1D framework based on spectral element method.
- A new element with embedded crack has been formulated in such a way that its introduction in a numerical procedure causes few disturbances.
- Due to the discrete nature of the proposed element, the slip concentration in regions adjacent to cracks is captured in a more realistic way, which allows controlling debonding failures in FRP-strengthened RC structures more properly.
- The model correlated well with test data globally and locally and can be used to predict IC debonding with confidence where debonding is governed by the bond–slip behaviour of the FRP-to-concrete interface.
- Due to its formulation, the proposed model is also able to capture the dynamic response, including high frequency response, of RC beams retrofitted with externally bonded FRP plates/sheets incorporating in a fast and simple way the influence on its behaviour of local phenomena, such as interfacial intermediate debonding, because of its ability to work accurately at high frequencies.

Acknowledgements

The writers acknowledge the support for the work reported in this paper from the Spanish Ministry of Economy and Competitiveness (Project BIA2010-20234-C03-01). Financial support for the CSC research fellowship given to Rui Sun and the FPI research fellowship given to Enrique Sevillano is also acknowledged.